RESEARCH ARTICLE

Crustal and uppermost mantle structure beneath western Tibet using seismic traveltime tomography

Ayda Shokoohi Razi[1], Vadim Levin[1], Steven W. Roecker[2], and Guo-chin Dino Huang[1]

[1]Department of Earth and Planetary Sciences, Rutgers University, 610 Taylor Rd., Piscataway, New Jersey, 08854-8066, USA, [2]Department of Earth and Environmental Sciences, Rensselaer Polytechnic Institute, Troy, New York, USA

Key Points:
- Crust of western Tibet is uniformly slow
- We find no evidence of a low velocity zone in the crust
- In the mantle, a fast narrow anomaly is consistent with the presence of eclogite

Correspondence to:
Ayda S. Razi,
shokoohi@eden.rutgers.edu

Abstract We study the elastic wave speed structure of the crust and the uppermost mantle in western Tibet using *P* wave and *S* wave arrival times from regional earthquakes recorded by a temporary seismic network. We relocate the earthquakes, and subsequently invert travel time residuals for 3-D distributions of wave speed. Resolution tests with a variety of input structures are used to verify the reliability of our results. The crust beneath western Tibet has low *P* wave speed (5.9–6.3 km/s) throughout its nearly 80 km thickness, with lower values in this range concentrated within the Lhasa block. Beneath the Himalaya wave speeds are higher. Southern and western limits of the slow material beneath the Tibetan Plateau correlate with the Karakoram fault, and dip beneath the plateau at ~40° angle. We find no evidence of a subhorizontal low velocity zone in the crust. In the uppermost mantle, we find a long and narrow region of fast (up to 8.4 km/s) *P* wave speed extending from the Karakoram fault in NE direction, and crossing the Bangong-Nujiang suture. In a north-south cross section, the distribution of relatively fast *P* wave speed suggests a ramp-flat geometry consistent with India underthrusting the Tibetan Plateau at least as far as 32.5°N. A plausible interpretation of the upper mantle fast feature is the formation of eclogite from the mafic lower-crustal material of India after it is underthrust beneath Tibet. Notably, in western Tibet this process only takes place in a narrow region.

1. Introduction

With an area of 2.5 million square km and an average elevation of more than 4500 m, the Tibetan Plateau is the largest, highest plateau on Earth [e.g., *Molnar and Tapponnier*, 1975; *Yin and Harrison*, 2000]. The plateau is a consequence of the convergence of the Indian and Eurasian plates, primarily since the early Eocene [e.g., *van Hinsbergen et al.*, 2011; *Royden et al.*, 2008] when the rate of convergence between India and Eurasia slowed rapidly from more than 100 mm/yr to about 50 mm/yr, presumably as a consequence of continents colliding when the intervening Tethys ocean was consumed [*Molnar*, 1984]. This ongoing collision has generated large crustal thicknesses (60–80 km) and major earthquakes along the edges of the plateau [e.g., *Yin and Harrison*, 2000; *Bilham*, 2004].

The Tibetan Plateau is composed of several distinct E-W oriented tectonic blocks formed at different times and in different conditions [*Yin and Harrison*, 2000]. Of particular interest to this study are the Lhasa and Qiangtang blocks (Figure 1). The Lhasa block is the southernmost block of the plateau. It extends about 2000 km in an E-W direction and is about 300 km wide. It is bounded to the south by the Indus-Yarlung suture (IYS) and is separated from the Qiangtang block to the north by the Bangong-Nujiang suture (BNS) [*Yin and Harrison*, 2000; *Murphy et al.*, 1997; *Kapp et al.*, 2003, 2007]. Both the Lhasa and Qiangtang blocks were parts of Gondwana before the late Paleozoic [*Kapp et al.*, 2003, 2007]. During the early Mesozoic, they separated from Gondwana and drifted northward, and by late Jurassic time, the Lhasa block collided with the Qiangtang block [*Yin and Harrison*, 2000; *Kapp et al.*, 2003]. Throughout the Cretaceous, the collision resulted in crustal shortening, thickening, and surface elevation gain in the Lhasa block [*Murphy et al.*, 1997; *Kapp et al.*, 2003, 2007].

The Tibetan Plateau has been studied intensely over the past few decades as a means to understand the first-order geodynamics of continental collisions. Among the debated issues involving this collision is the role of the underthrusting of the Indian lithosphere in the shortening and support of the Tibetan Plateau, in particular whether it underplates the entire plateau or sinks into the mantle [e.g., *Kosarev et al.*, 1999; *Li et al.*, 2008]. A related set of issues concerns the amount and fate of consumed Indian crust: whether a
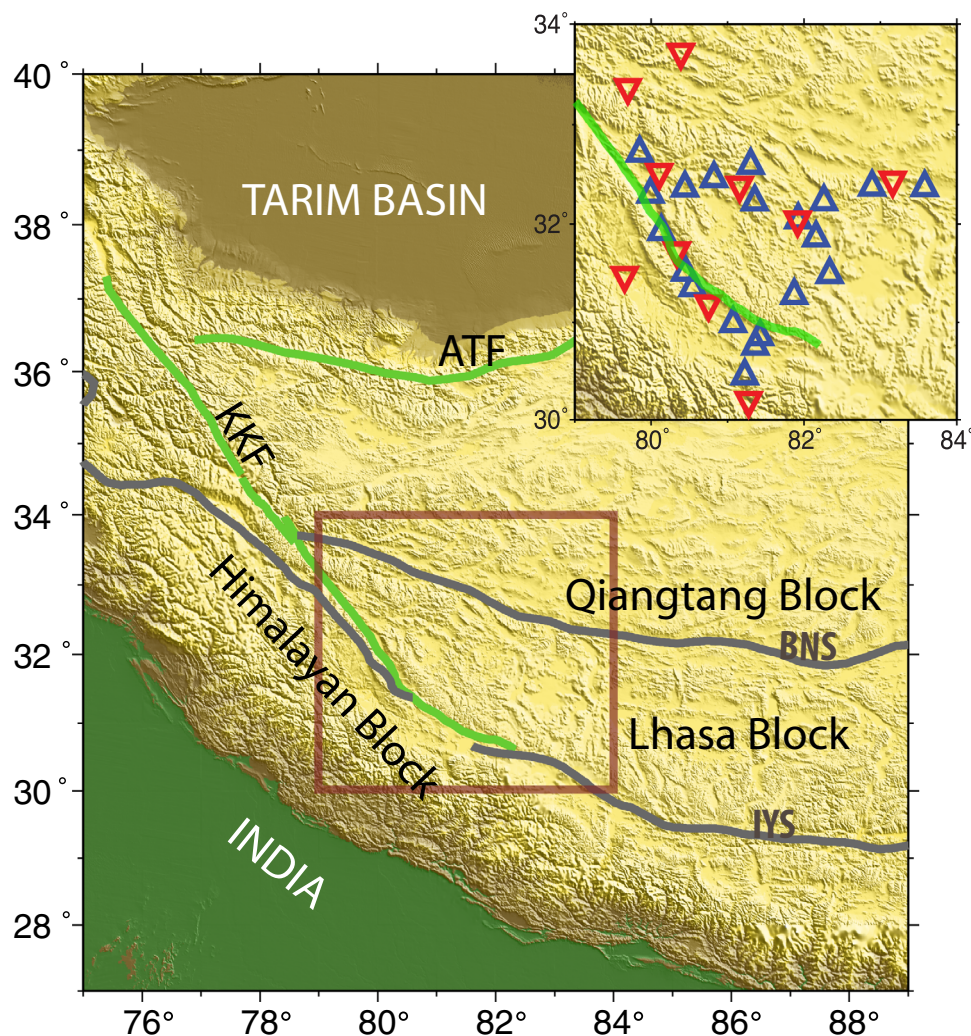
Figure 1. Tectonic map of western Tibet and surrounding areas showing the Himalayan, Lhasa and Qiangtang blocks, two suture zones (IYS: Indus-Yarlung suture and BNS: Bangong-Nujiang suture), and two major faults (KKF: Karakoram fault and ATF: Altyn Tagh fault). Brown box shows the main area of investigation. Inset shows the location of seismic stations used for this study. Red triangles locate seismic stations deployed in the summer of 2007. Blue triangles locate additional seismic stations deployed in August 2009.

significant amount of it is underthrust with the rest of the Indian lithosphere, whether it is responsible for the doubling of crustal thickness, and whether it perhaps undergoes a transformation to higher density eclogite [*Huang et al.*, 2009; *Nabelek et al.*, 2009]. Other questions concern the rheological state of the Tibetan crust itself, in particular the potential for channel flow in the mid to lower crust which could result in the flow of the Tibetan crust outward [*Copley and McKenzie*, 2007; *Royden et al.*, 2008], and that may be returning material into the Himalaya [*Burchfiel and Royden*, 1985; *Searle et al.*, 2011], implying an exchange of material between India and the Tibetan Plateau.

Many of these scenarios can be tested through the subsurface imaging of elastic properties that result from seismic investigations, and accordingly numerous arrays of seismic sensors have been deployed across the eastern, northern, and southern sides of the Tibetan Plateau in the past two decades [e.g., *Li et al.*, 2006; *Zhang et al.*, 2011]. However, due to the remoteness, difficult working conditions, and political sensitivity of the region, few detailed seismological studies have examined the western part of Tibet. Hence, the structure of this part of the plateau is poorly known.

From 2007 to 2011, a US-China collaborative data collection effort took place in western Tibet. With 4 years of data, this is the longest temporary regional network operated across the Tibetan Plateau. During this time, a number of large earthquakes (magnitudes 6–7.3), accompanied by numerous aftershocks, took place

close to the study region. The resulting data set offers an excellent opportunity to probe crustal and upper-most mantle structure in the region.

In this paper, we investigate the crustal and uppermost mantle structure beneath western Tibet in order to understand the dynamic process of the western margin of the Tibetan Plateau. The *P* wave and *S* wave arrival times from regional earthquakes are used to image the velocity structure and to relocate regional events in the study region. In the following sections, we discuss past geophysical studies of the region, describe the details of the seismic tomography inversion and quality control methods used in this study, and discuss our findings in the context of the geological structure of the region.

2. Previous Studies in Western Tibet

Seismological studies of the crustal structure in the vicinity of western Tibet include a number of refraction lines [*Zhang et al.*, 2011], receiver functions studies based on a Sino-French data set [*Wittlinger et al.*, 2004], more recent investigations associated with the Hi-Climb project [*Basuyau et al.*, 2013; *Griffin et al.*, 2011; *Nabelek et al.*, 2009], and analyses of dispersion of both ambient noise and ballistic surface waves [*Rapine et al.*, 2003; *Caldwell et al.*, 2009; *Sun et al.*, 2010].

Estimates of crustal thickness in the region vary from 70 to 75 km [*Zhang et al.*, 2011; *Nabelek et al.*, 2009; *Griffin et al.*, 2011] to nearly 90 km [*Wittlinger et al.*, 2004]. Refraction studies report compressional seismic velocities in 6.0–6.4 km/s range, while studies of the ambient noise and surface wave dispersion find crustal shear wave speeds in the 3.2–3.6 km/s range [*Caldwell et al.*, 2009; *Sun et al.*, 2010; *Yang et al.*, 2010], with some evidence for a low velocity zone in the midcrust. *Rapine et al.* [2003] report faster (∼3.8 km/s) shear wave speeds in the lower crust of the Lhasa block.

Dricker and Roecker [2002] documented significant differences in the upper mantle structure between the eastern and western parts of the Tibetan Plateau. In the west, they found the upper mantle to have higher shear wave speeds in the upper 200 km. Similarly, tomographic imaging of compressional velocity by *Li et al.* [2008] outlined a region of high-compressional velocity beneath western Tibet, extending from the Himalaya mountains to the IYS at depth ∼100 km, and even further to the north-east at larger depths.

A number of studies find evidence for underthrusting of Indian lithosphere beneath the Tibetan Plateau [*Kosarev et al.*, 1999; *Li et al.*, 2008]. However, recent work from the Hi-Climb project [*Basuyau et al.*, 2013], using joint inversion of teleseismic and gravity data, suggested a near-vertical descent of the Indian litho-sphere beneath the center of the Tibetan Plateau. Their findings indicate that the Indian lithosphere is located between IYS and BNS at a depth of ∼400 km. Other studies analyzed deep earthquakes and tomo-graphic images to investigate the structure of the Indian lithosphere beneath the Tibetan Plateau [*Huang et al.*, 2009; *Nabelek et al.*, 2009]. Their results suggested the presence of eclogitized lower crust of India beneath the Himalaya and southern part of Tibet.

Several studies inferred the presence of channel flow within the crust of the eastern and southern margins of Tibet [*Klemperer*, 2006; *Nelson et al.*, 1996; *Royden et al.*, 2008; *Copley and McKenzie*, 2007]. Geodetic results are used to propose the presence of channel flow spreading the crustal material outward from the Tibetan Plateau [*Copley and McKenzie*, 2007; *Royden et al.*, 2008], while structural geology arguments are used by *Burchfiel and Royden* [1985] and *Searle et al.* [2011] to infer a return flow of crustal materials from beneath Tibet into the Himalaya. At the same time, recent studies in the western part of Tibet argued that the long-lived strike-slip Karakoram fault (KKF) acts as a barrier to such flow, both presently and in the recent (20 Ma) geological past. *Leech* [2008] combined the timing of granitoid volcanism and results of seismic and magne-totelluric studies along the KKF to argue that it blocked channel flow into the western Himalaya. *Klemperer et al.* [2013] used helium isotopes signatures of geothermal hot springs along the KKF to suggest that it penetrates into the mantle. This scenario would be incompatible with both the channel flow from Tibet back into Himalaya, and the underthrusting of the Indian crust beneath Tibet.

3. Data

As part of a US-China collaborative data collection effort, we operated an array of broadband seismic sta-tions in western Tibet from July 2007 to May 2011. The study described in this paper is based on the analy-sis of data collected during the first 3 years. The network consisted of 8–10 sites during its first 2 years and
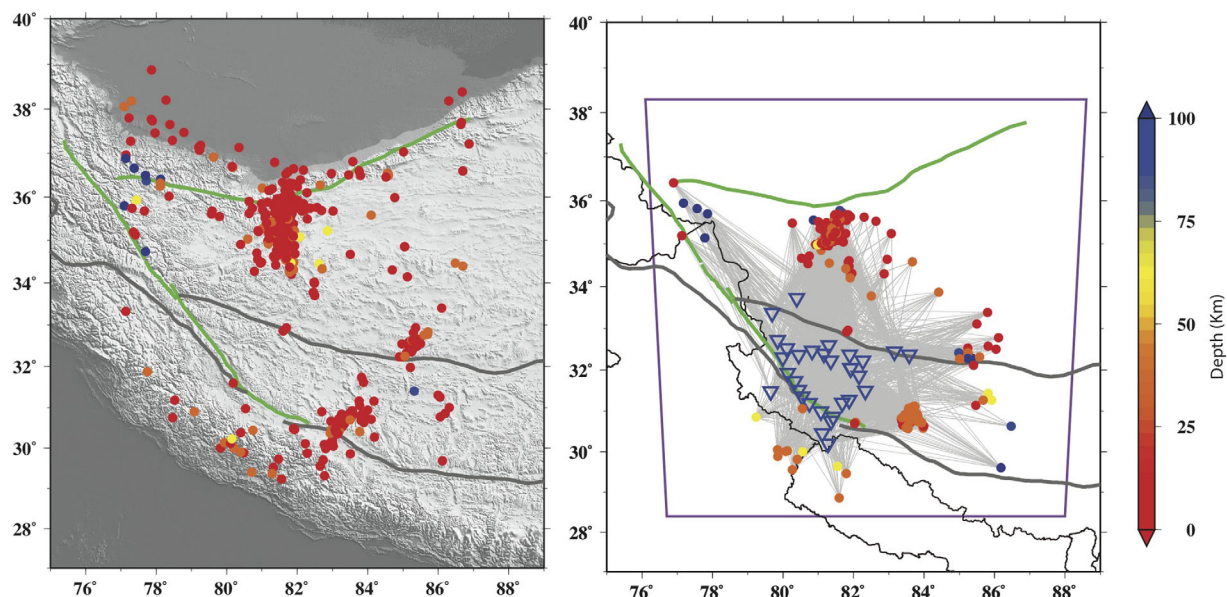
Figure 2. (left) Epicenters (color coded by depth) of 513 earthquakes with $M > 3$ from July 2007 to July 2010 reported in the CEA catalog. (right) 282 relocated earthquakes and corresponding raypaths. Raypaths are presented with light gray lines. Dark gray lines locate the IYS and BNS sutures; green lines are the Karakoram and Altyn Tagh faults. Purple box shows the volume of our model. Blue triangles are seismic stations. Black lines are political boundaries.

30 sites in the third year (Figure 1, inset). We used the China Earthquake Administration (CEA) catalog (http://data.earthquake.cn) to identify time windows of earthquakes with magnitude 3.0 and larger that took place close to the network, specifically between 29°N and 39°N in latitude, and between 77°E and 87°E in longitude. We examined records of 513 events that occurred from July 2007 to July 2010 (Figure 2). In March of 2008, an $M = 7.3$ earthquake occurred near the Altyn Tagh fault (ATF) on the northern border between Tibet and the Tarim Basin and was followed by numerous aftershocks. Four more events with magnitudes over 6.0 took place in this time period between 83°E and 86°E in longitude, each followed by a sequence of aftershocks. Hence, our data set is dominated by events from three distinct source regions, one to the north of the network, and two to the east and south-east of it (Figure 2). In the eastern and southeastern parts of our study area, events are recorded only in the last 2 years, while in the northern part earthquakes are reported over the entire 3 year period. Most of the earthquakes have shallow (<40 km) sources. However, a few intermediate depth (70–195 km) earthquakes, most likely associated with the Pamir seismic zone, are reported around the intersection of KKF and ATF between 77°E and 78.5°E in longitude, and between 34°N and 37°N in latitude. After a visual inspection of seismograms, we selected 282 events that were recorded with a high signal-to-noise ratio on at least four stations. We manually picked the arrival times of P waves and S waves (2496 and 1035, respectively) and assigned a global time uncertainty (0.2 s for P waves and 0.6 s for S waves) based on our assessment of the records.

4. Methodology

We invert the observed P wave and S wave arrival times using the finite difference arrival time tomography algorithm described in *Roecker et al.* [2004, 2006] to obtain 3-D velocity models. Because the region of interest is large (1100 km × 1100 km), we compute travel times using an adaptation of an eikonal equation solver directly to a spherical coordinate system [e.g., *Zhang et al.*, 2012]. Wave speeds for both P waves and S waves are specified on a grid, which in our case consists of 111 × 111 × 23 nodes in the N-S, E-W, and vertical directions, respectively, spaced at 10 km. Station elevations are 4500 m on average; differences in elevation are accounted for by embedding the stations in the model volume that extends 30 km above the sea level.

The arrival time tomographic inversion involves two principal steps. The first relocates regional earthquakes in a starting model through an interpolated grid search. The second calculates raypaths from all sources to recording stations to evaluate partial derivatives of travel times with respect to model parameters. These

form a system of linear equations that is then solved using a damped least squares approach. The resulting perturbations to P wave and S wave speeds are added to the current model. These two steps are repeated until the variance reduction between two successive iterations becomes small.

Following a procedure successfully applied by *Huang et al.* [2009], the linearized inversion is heavily damped to promote stability and mitigate artifacts. Moreover, after each iteration the perturbations are smoothed over the nearest five lateral nodes and three vertical nodes. This type of a posteriori smoothing helps reduce the appearance of short wavelength perturbations that are not required by the data.

5. 1-D Velocity Model and Earthquake Relocation

We adopted a progressive approach to our inversion by starting with a simple model with few parameters and introducing more complicated models as required by the data. In particular, we began by first selecting those events with the best-constrained locations, and then using the observations from these events to recover a best fitting 1-D model. We then used this 1-D model as a starting point for a 3-D inversion. We performed single-iteration relocations of selected 282 events, seeking a 1-D model with lowest misfit variance. We started with a single crustal layer over a half-space, and tested a range of values for the crust Vp (5.7–6.4 km/s), the mantle half-space Vp (7.8–8.2 km/s), the Vp/Vs ratio (1.7, 1.75, 1.8), and the Moho depth with respect to sea level (65–90 km). Attempts to find a model with two layers over a half-space that would fit better than a one-layer model were not successful. The chosen model for initial earthquake relocation had the following parameters: crustal Vp = 6.2 km/s, crustal Vp/Vs ratio = 1.77, mantle Vp = 8.1 km/s, mantle Vp/Vs ratio = 1.88, and a Moho depth of 75 km. Given that in Tibet the average elevation of our stations is ∼4.5 km, this implies a crustal thickness of nearly 80 km.

Compared to the original CEA locations, relocated hypocenters in the 1-D model are more clustered in the northern and eastern parts of the study region (Figure 2). Most of the relocated earthquakes have hypocentral depths less than 40 km. However, a small number of earthquakes with CEA catalog depth over 40 km remain deep.

Almost all earthquakes in our data set are outside the network (Figure 2), and based on the CEA catalog, most appear to have upper crustal depths. Consequently, practically all of the rays are downgoing at the source, and our inverse procedure resembles those that analyze Pn-type phases [e.g., *Hearn*, 1999]. In this case, epicenters of these events can be stable, but origin times and depths will be strongly coupled. Hence, we fixed all hypocenters after relocating them in the chosen 1-D model.

We found that events with small numbers (<6) of picks generated very large delays, which is likely a result of poor control on the hypocentral location. Hence, the earthquakes included in the 3-D inversion were required to satisfy the following criteria: (1) a minimum of eight phase picks, (2) a standard deviation of the P wave and S wave traveltime residuals less than 3 s, and (3) for individual picks, travel time residuals less than either 10 s or 5% of the total travel time. After applying these criteria, 2243 P wave and 998 S wave traveltime observations from 234 events remained for the analysis.

6. 3-D Velocity Inversion

As discussed above, we heavily damped our inversion to mitigate artifacts. We tested a range of damping values and chose a value of 1000 that allowed our model to change by small amounts at any iteration. We also attempted to decrease the damper gradually at later stages in the inversion as described in *Huang et al.* [2009]; however, the outcome was not significantly different. After 40 iterations, the amount of variance reduction between two successive iterations became smaller than 0.04% (Figure 3), and the change in velocity perturbations was also negligible (<0.01%). The overall variance reduction relative to the initial 1-D model was 22%. A plot of the delays for both P waves and S waves after 40 iterations (Figure 4) shows a distribution of P wave residuals tightly clustered around zero. The histograms of the arrival time residuals for both P waves and S waves after 40 iterations are biased with nonzero negative means, i.e., on average the observed travel times are smaller than the predicted travel times. The majority of the misfits for P waves are in the −1 to 1 s interval, while S waves delays are about twice as large. Partly this reflects the greater uncertainty of the S wave picks, which leads to their influence being more heavily damped in the inversion. This likely results in the small changes to S wave speeds we get in the final model.
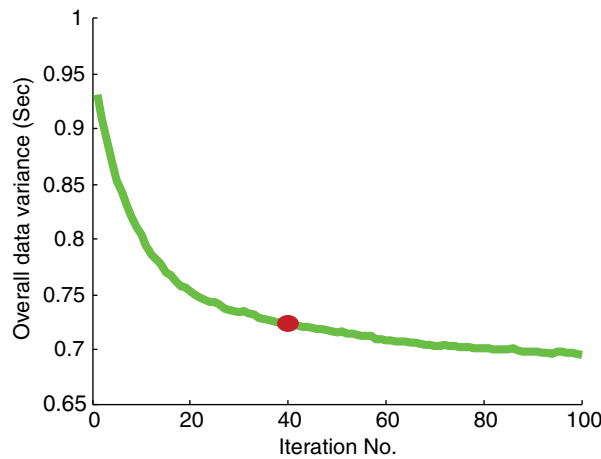
Figure 3. Overall variance reduction with respect to the initial 1-D model as a function of iteration number. The inversion stops after 40 iterations (red dot), beyond which model perturbations and reductions in variance are small.

The mean P wave speeds are 6.2 km/s in the crust and 8.1 km/s in the uppermost mantle; the same as those found in the best fitting 1-D model. The mean S wave speeds are 3.5 km/s and 4.3 km/s in the crust and the mantle, respectively. The inversion for P wave and S wave speed was carried out independently; however, final mean values did not change from the starting 1-D model. An inversion using Vp/Vs ratios instead of S wave speeds yielded nearly identical results.

Within the final 3-D model (Figure 5), we see P wave speed anomalies up to 5% in a region approximately corresponding to the area covered by our network. The depth extent of the volume with anomalies recovered is ∼120 km. Significantly, our inversion does not alter the mean velocity outside the area covered by the stations, thus we do not expect features far outside our network to influence the anomalies we recover. S wave speed anomalies in the 3-D model are very weak, under 1% in the crust, and under 2% in the mantle, and are not shown. Anomalies of P wave speed have significantly different shapes in the crust and the upper mantle (Figure 5). A change in the shapes of the anomalies happens between the depths of 70 and 80 km, a depth range where the best-fitting 1-D model indicates a transition from crust to mantle wave speeds.

7. Observational Geometry and Velocity Control

The unusual geometry of our data set presents a number of challenges. The volume where raypaths from different sources cross is restricted to a small region beneath the seismic network. Consequently, for most observations the bulk of the travel time delay is accumulated outside this volume and is likely to transfer the influence of the outer parts of the model space toward the center. Also, because the earthquakes we use in our analysis are located outside of the aperture of the network, one may expect some trade-off between wave speeds and hypocenters in a fashion similar to teleseismic arrival time analysis, and hence a lessened sensitivity in our observations to absolute wave speeds. While some trade-off is unavoidable, a difference between our situation and that of teleseismic observations is that the raypaths are not parallel; specifically, they combine waves passing though the crust with refracted Pn and Sn. Hence, our situation is
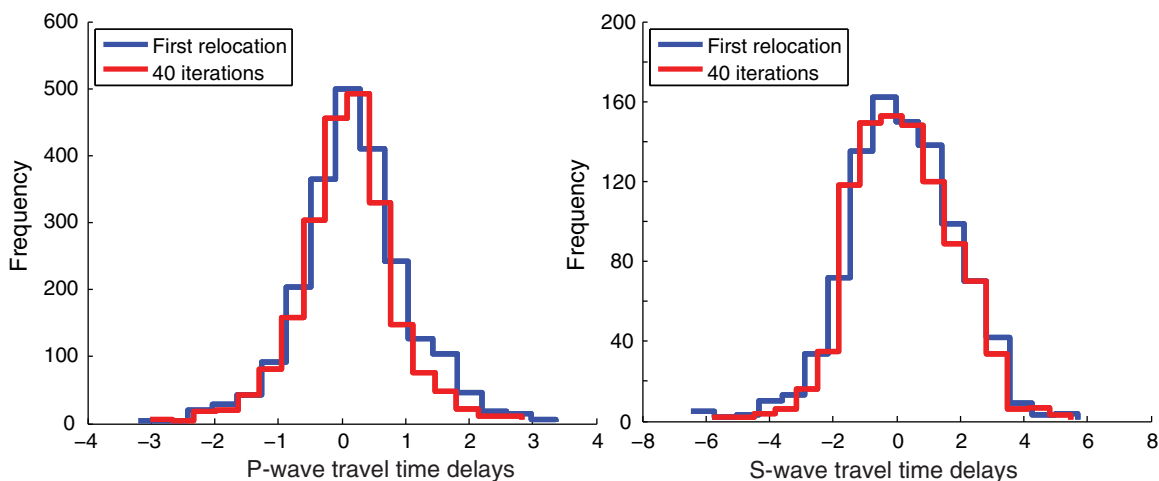

Figure 4. Distribution of travel time residuals after first relocation (blue line) and after 40 iterations (red line) for (left) P wave and (right) S wave.
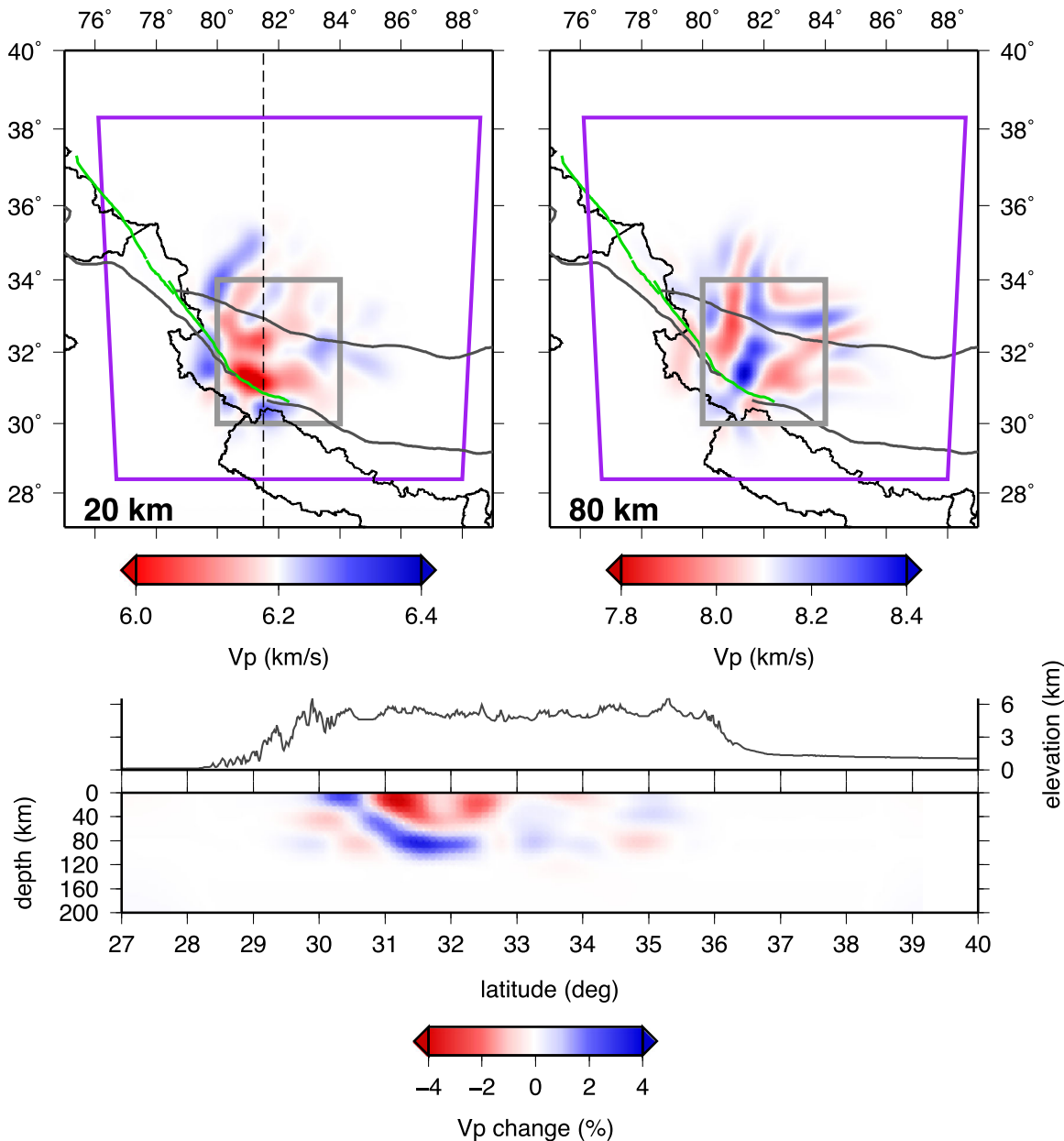
Figure 5. Results of the 3-D tomographic inversion for the entire model shown by horizontal sections at (top left) 20 km and (top right) 80 km depths for *P* wave structure, and cross section (no vertical exaggeration) along N-S direction (bottom) at 81.5°E. Dash line in the top left locates the cross-section. Gray box indicates the well-resolved area, as suggested by resolution tests. Map symbols are shown in Figures 1 and 2.

more similar to refracted wave analysis, where sensitivity to absolute wave speeds in the upper mantle is retained. We explored the degree to which absolute velocity values can be recovered, the influence of outer areas of the model on its center, and the resolution of lateral and vertical changes in wave speed by conducting a series of tests described in section 8. For the most part, we find that our data set is capable of recovering absolute wave speeds to within a percent. In the upper mantle, the lateral extent of both fast and slow anomalies is recovered well. Within the crust, we recover shapes of the fast anomalies better than those of the slow anomalies.

8. Resolution Tests

In order to assess the degree to which our data are capable of resolving heterogeneity in the crust and the upper mantle, we performed several resolution tests. We started with a variation on the standard
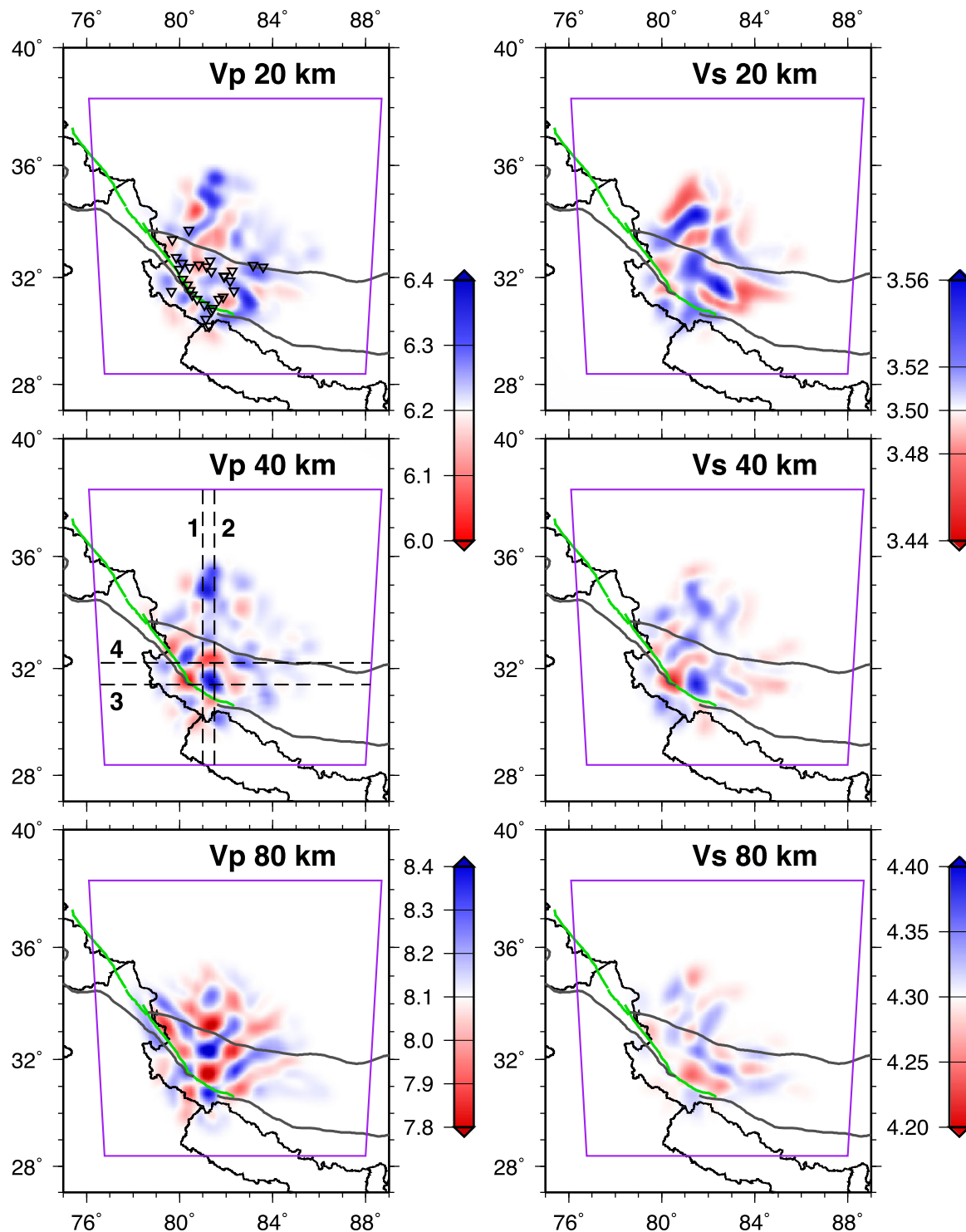
Figure 6. Horizontal slices through results of the checkerboard resolution test with fixed hypocenters (left column) for *P* wave and (right column) for *S* wave at 20, 40, and 80 km depths, respectively. Dash lines identify locations of the cross sections shown in Figures 7 and 14. Map symbols are shown in Figures 1 and 2.

checkerboard tests by constructing a set of models with 5% velocity anomalies of alternating sign (Figures 6 and 7). Checkers are 70 km long and 20 km thick, separated by gaps of 30 km and 20 km in horizontal and vertical directions, respectively. Tests with shorter dimensions were not recovered well with our data set; hence, these dimensions represent a resolution limit for our data set.
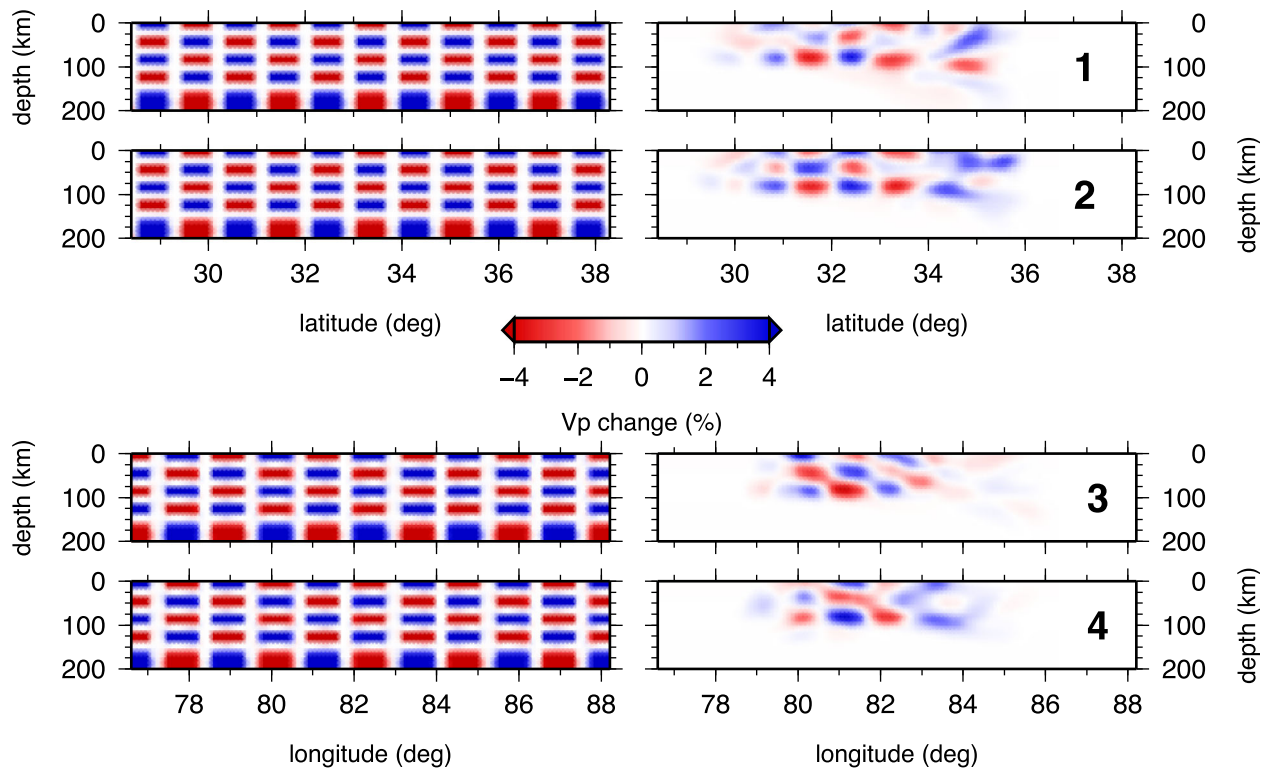
Figure 7. N-S and E-W cross sections (no vertical exaggeration) of the checkerboard test for *P* wave speed along (1) 81°E, (2) 81.5°E, (3) 31.4°N, and (4) 32.2°N. Locations of the cross sections are shown in Figure 6. Plots on the left show the initial checkerboard models, with alternating fast and slow anomalies of 5%. Output model for each cross section is shown on the right.

Synthetic traveltimes were computed in the model for all stations and sources, and then analyzed in the same way as the real data. Hence, we fixed the hypocentral parameters of all sources after the first relocation, and solved for velocities only in subsequent iterations. After testing a range of damper values, we found that we have a better variance reduction with a damper value of 100. We stopped the inversion after 15 iterations, at which point the variance was reduced by 64%.

To determine the potential effects of fixing hypocenter locations after the first iteration on our results, we repeated the checkerboard test above and allowed the hypocenters to relocate after every iteration. The result of this test (supporting infomation Figure 1) is similar to the one with fixed hypocenters, suggesting that the decoupling between hypocenters and wave speeds is sufficient to allow us to resolve structure at this level of detail. As may be expected, a much larger variance reduction of 92% is achieved when the hypocenters are adjusted; this behavior mimics the modest variance reduction achieved in the real data when hypocenters are fixed.

Results for the checkerboard tests (Figures 6 and 7) show that resolution is good (i.e., the shape and amplitude of the input velocity pattern is recovered) for *P* wave speed anomalies between 30°N and 34°N in latitude, and between 80°E and 84°E in longitude, i.e., within the area covered by stations. At the same time, resolution in cross-section 2 (longitude 81.5°E) is better than that in cross-section 1 (longitude 81°E), and that in the cross-section 3 (latitude 31.4°N) is better than in cross-section 4 (latitude 32.2°N) (Figure 7).

Horizontal sections (Figure 6) indicate that the model is well resolved throughout most of the crust but is poorly resolved at depths less than about 20 km. Beneath the crust, individual checkers are well resolved down to depths of ∼100 km. *S* wave speeds are not well resolved by this data set (Figure 6), which could explain the lack of variation in S velocity in our tomographic images.

We constructed a variety of synthetic models with 5% velocity anomalies for *P* wave speed in both the crust and the upper mantle to assess the resolution of anomalies with shapes and dimensions of particular
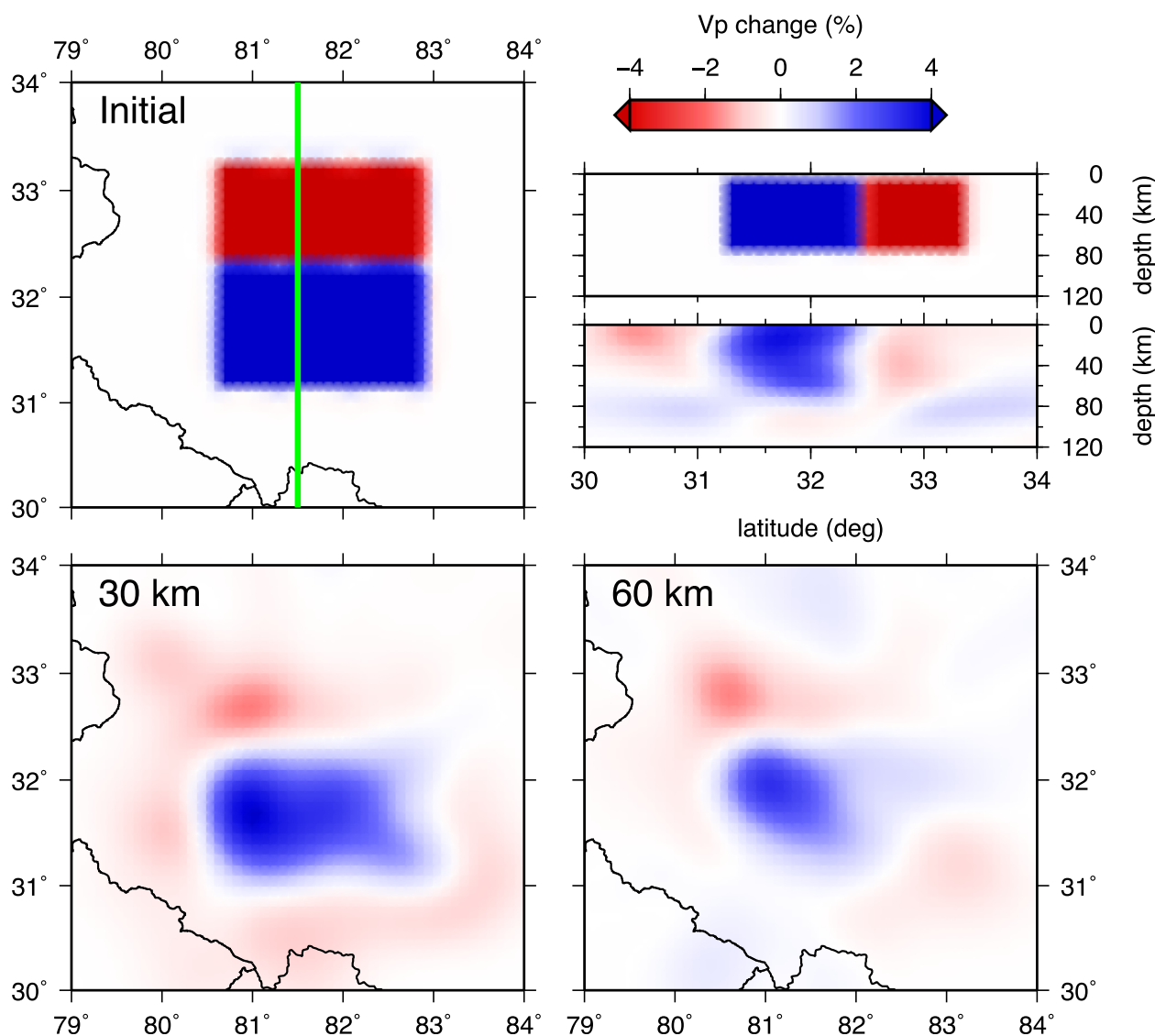
Figure 8. Example of resolution test of lateral variations of *P* wave velocity in the crust. Input model for (top left) *P* wave velocity at 30 km depth, (bottom left) *P* wave velocities at 30 km depth after 40 iterations, and (bottom right) *P* wave velocities at 60 km depth after 40 iterations. Cross section (no vertical exaggeration) of the input *P* wave velocity model (top right) at 81.5°E, and the result of the inversion after 40 iterations. Green line in the top left plot locates the cross section. Black lines are political boundaries.

relevance to our interpretation (Figures 8–11). For each resolution test, as with the real data, we carried out 40 iterations. At this point, the change in variance between two successive iterations is small in all cases.

In our first synthetic model, we define two large blocks with high and low speeds (Figure 8) to test resolution of north-south velocity changes in the crust. The blocks are 60 km thick (10–70 km depth). The results show that the fast anomaly is well recovered in the area covered by our stations (approximately between 31.2°N and 32.5°N in latitude), while the slow anomaly (which is located mostly outside the network) is only partially recovered and smeared somewhat to the north. The high velocity block is resolved better at mid-crustal depths (e.g., 30 km) than in the lower crust (e.g., 60 km).

In the second model, we test the resolution of east-west velocity changes in the crust. We define a pair of fast and slow velocity anomalies between 31.2°N and 34.6°N in latitude, and between 80.4°E and 83.6°E in longitude (Figure 9). Both anomalies are ~200 km long and 60 km thick, from 10 to 70 km in the vertical direction. Results for the *P* wave structure along the east-west cross section at 32.0°N latitude show that the model is well resolved within the area covered by stations. The reconstructed slow anomaly is much weaker between longitudes of ~82.5° and ~83.5°E, and a few minor wave speed artifacts appear around the high
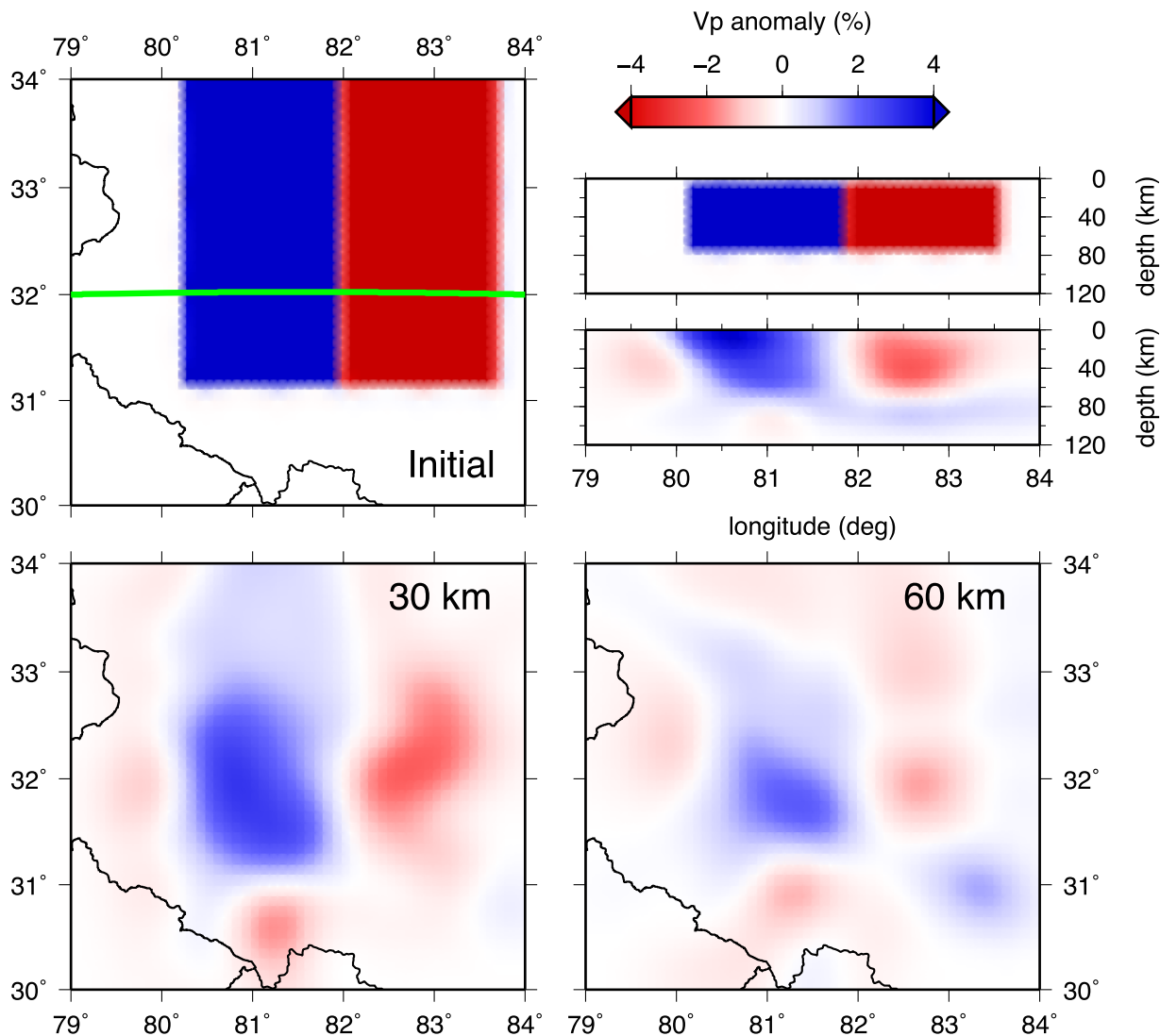
Figure 9. Resolution test of lateral variations of P wave velocity in the crust. Input model for (top left) P wave velocity at 30 km depth, (bottom left) P wave velocities at 30 km depth after 40 iterations, and (bottom right) P wave velocities at 60 km depth after 40 iterations. Cross section (no vertical exaggeration) of the input P wave velocity model (top right) at 32.0°N, and the result of the inversion after 40 iterations. Green line in the top left plot locates the cross section. Black lines are political boundaries.

velocity block both in the shallow and the deep parts of the model. Nevertheless, the boundary between the two blocks is well resolved. The bottoms of both the fast and the slow blocks are somewhat smeared. This test shows that the east-west lateral resolution is good in the area covered by our network but that minor artifacts can be present at the edges of the model.

Our third test is designed to see whether a low velocity zone in the middle of the crust beneath our study may be resolved. We define a low velocity anomaly from 81.2°E to 82.5°E in longitude, and from 31.5°N to 32.6°N in latitude (Figure 10), which is within the area covered by the network. The thickness of this low velocity feature is 30 km, extending from 20 to 50 km depth. Results for the P wave structure along the north-south cross section at the longitude of 81.5°E show that while the amplitude of the anomaly is underestimated, the region of low velocity is well constrained beneath our study area. It is also better resolved at shallower depths (e.g., depth of 30 km), and there is some downward smearing to 60 km. Again, mild artifacts (higher wave speeds not present in the input structure) appear at the edge of the recovered low velocity anomaly.

In our fourth test, to evaluate model resolution in the uppermost mantle we define a high velocity feature between 30.6°N and 33.2°N in latitude, and between 80.2°E and 83.2°E in longitude, extending from 80 to
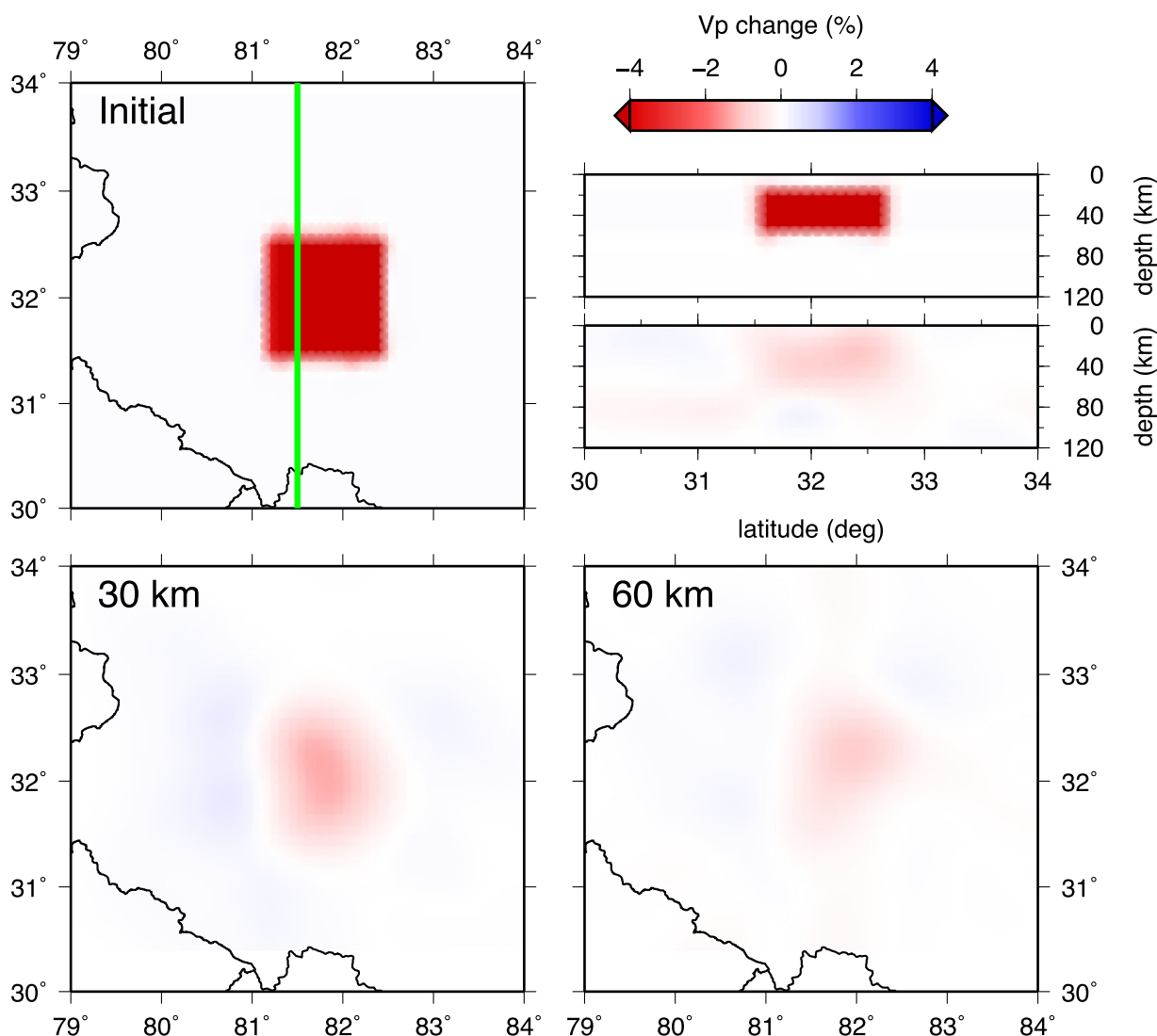
Figure 10. Resolution test of the low *P* wave velocity zone in the middle crust. Input model for (top left) *P* wave velocity at 30 km depth, (bottom left) *P* wave velocities at 30 km depth after 40 iterations, and (bottom right) *P* wave velocities at 60 km depth after 40 iterations. Cross section (no vertical exaggeration) of the input *P* wave velocity model (top right) at 81.5°E, and the result of the inversion after 40 iterations. Green line in the top left plot locates the cross section. Black lines are political boundaries.

110 km depth (Figure 11). A north-south cross section at 81.5°E shows that while the high velocity feature is a little smaller and thinner in the reconstruction, it is fairly well constrained beneath the study area. As in the other tests, artifacts can be seen at the edges of the input anomaly, especially in the northeastern (between ∼83.2°E and 84°E in longitude, and between 32.54°N and 33°N in latitude) part of the model. This result suggests that our tomographic inversion should be able to resolve a similar high velocity feature directly beneath the crust-mantle transition, but also that resolution is poor at depths greater than about 110 km.

Finally, in order to test the resolution of the features suggested by the actual inversion, we perform a restoration test in which the input model is our final 3-D velocity structure (Figure 5). Results of the restoration test (Figure 12) show that while shapes of most features in the region covered by our stations are well recovered, the strength of anomalies is underestimated.

In summary, our resolution tests show that our inversion results are reliable in the area between 30°N and 34°N in latitude, and between 80°E and 84°E in longitude. We expect some minor artifacts outside this area. We are able to resolve lateral structures of at least 70 km in dimension. Our data can resolve fast
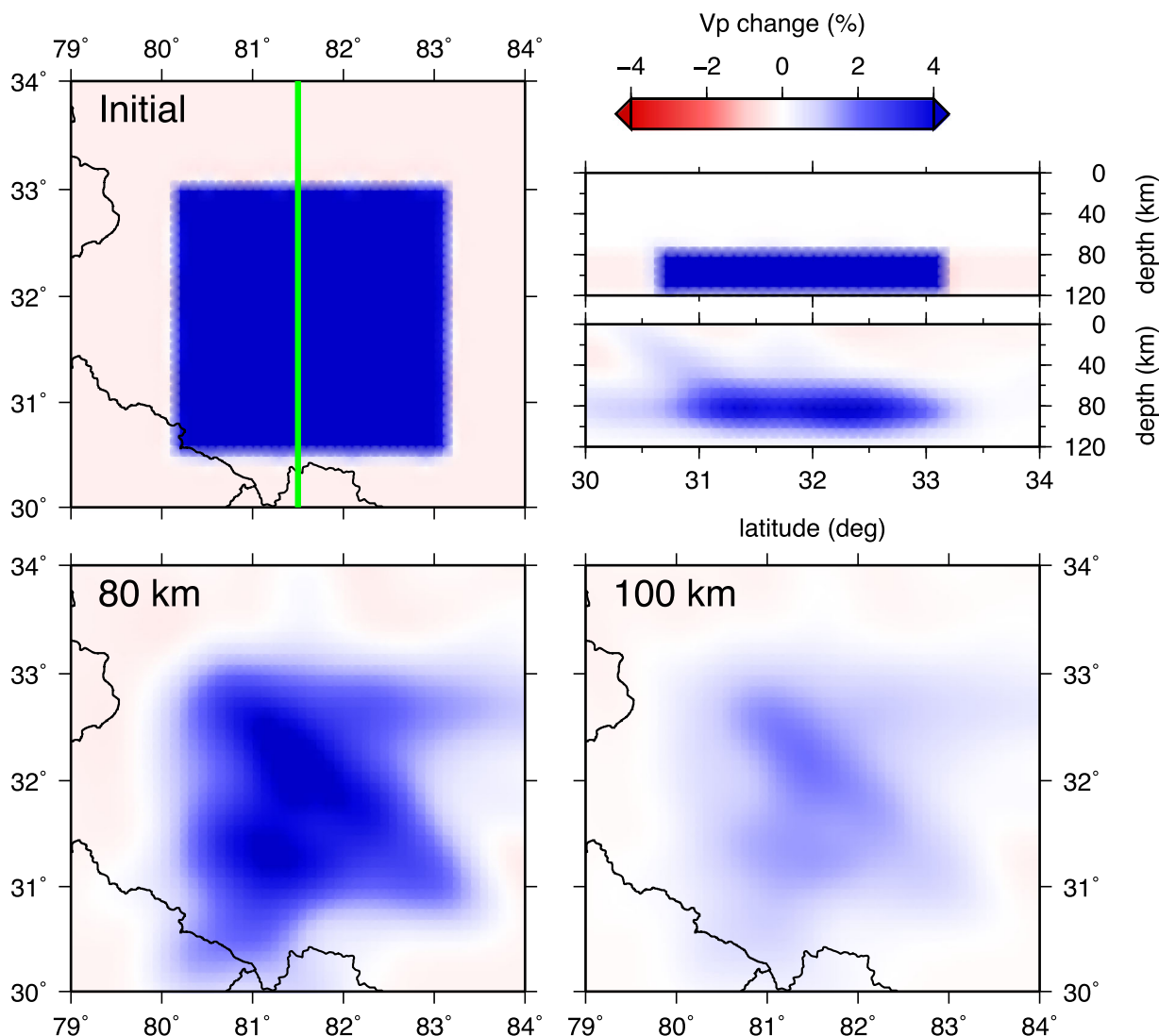
Figure 11. Resolution test of the high *P* wave velocity zone in the uppermost mantle. Input model for (top left) *P* wave velocity at 80 km depth, (bottom left) *P* wave velocities at 80 km depth after 40 iterations, and (bottom right) *P* wave velocities at 100 km after 40 iterations. Cross section of the input *P* wave velocity model (top right) at 81.5°E, and the result of the inversion after 40 iterations. Green line in the top left plot locates the cross section. Black lines are political boundaries.

anomalies in both the crust and the uppermost mantle; however, we expect the amplitudes of the anomalies to be underestimated. Slow anomalies can be resolved in the midcrust, but the recovered low velocity anomaly may spread vertically. Finally, we do not expect to be able to resolve any structure below ~110 km depth.

9. Features of the Final 3-D Model

In Figures 13 and 14, we present maps and cross sections of the *P* wave speed distribution in the well-resolved central part of our model. A strong slow anomaly dominates the crust of Tibet, while areas beneath the Himalaya are faster. Patterns of anomalies within the uppermost mantle (Figure 13) are very different from those in the crust, with an elongate (100 km × 400 km) fast anomaly surrounded by two slow features extending from SW to NE. A slow anomaly extends westward for ~300 km, and a separate minor slow anomaly is located to the east.

Vertical cross sections (Figure 14) show mostly low wave speeds beneath Tibet, and a region of high wave speed beneath the Himalaya. The boundary between the areas of low and high wave speed is either at, or just to the south of, the KKF, and dips ~40° northward. The fast velocity anomaly in the crust merges with a
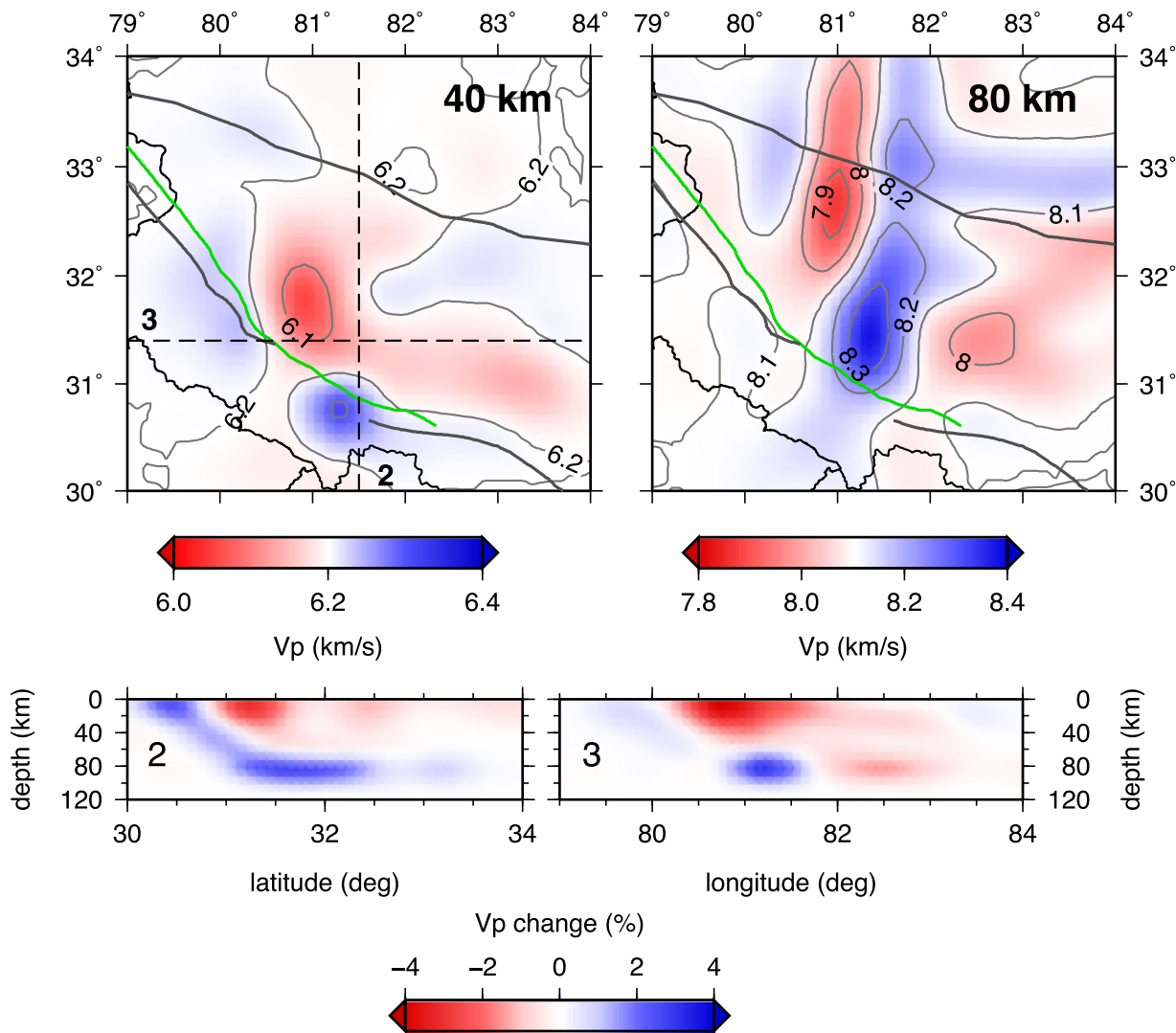
Figure 12. Results of the restoration test for the *P* wave speed at depths of (top left) 40 km and (top right) 80 km and along cross sections (no vertical exaggeration) at (bottom left) 81.5°E and (bottom right) 31.4°N. The locations of the cross sections are shown in the top left plot. Contour lines indicate absolute *P* wave speeds at intervals of 0.1 km/s. Map symbols are shown in Figures 1 and 2.

horizontal fast anomaly beneath the Moho (cross-section 2 in Figure 14), forming a ramp-flat shape that extends to ~32.5°N. A similar fast anomaly in the crust is seen farther to the west (cross-section 1 of Figure 14), where it extends only to ~32°N. The slow anomaly within the Tibetan crust merges with a slow feature in the uppermost mantle. A near-surface area of especially low velocities underlies the traces of the KKF and IYS. A small fast anomaly is also seen in the northern part of the cross-sections 1 and 2, apparently beneath the BNS. The strength of the fast velocity anomalies is higher in the eastern cross section, while slow anomalies are similar in strength throughout the region. Areas south-west of the KKF are characterized by fast velocities down to ~50 km. The association of the boundary between fast and slow anomalies and the surface geology (e.g., traces of KKF and IYS) is less obvious in these sections. The boundary between slow and fast areas in cross-section 3 (Figure 14) appears to dip eastward at ~40°, similar to the contact in cross-sections 1 and 2. This boundary is less clear farther to the north in cross-section 4. In the southern cross section, the near-surface area of low velocities is restricted to the upper crust, while in the northern cross section low velocities extend through the lower crust and into the uppermost mantle.

To summarize, the crust of western Tibet appears to be uniformly slow, while that beneath the Himalaya is fast. The contact between these crustal regions of fast and slow speed follows the trace of the KKF, and appears to be dipping to the north and east. In contrast, the uppermost mantle is characterized by a long,
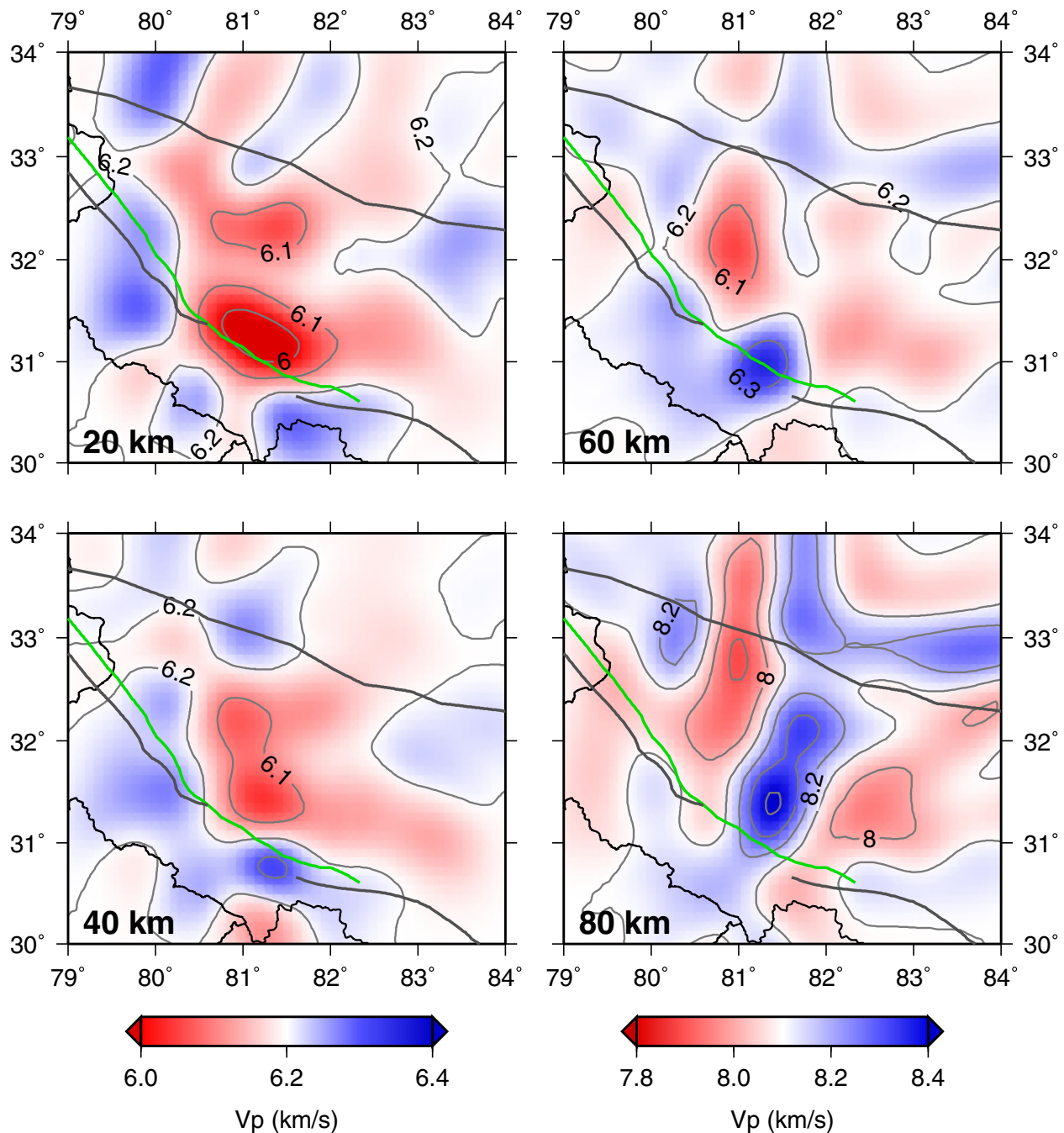
Figure 13. Results of the 3-D tomographic inversion in the well-resolved areas for *P* wave structure shown by horizontal sections at (top left) 20 km, (bottom left) 40 km, (top right) 60 km, and (bottom right) 80 km depths. Map symbols are shown in Figures 1 and 2. Contours are identical to Figure 12.

narrow fast anomaly that appears to crosscut both the KKF and the BNS. A prominent slow anomaly to the west of this feature also crosses the BNS, but appears to stop at the KKF. Maps of *P* wave speeds in the crust are characterized by a central slow anomaly, with values between 5.9 and 6.1 km/s, bounded on the south, along the IYS, as well as west of 80°E by velocities up to 6.3 km/s.

10. Discussion

Our best estimate of a 1-D model for western Tibet gives a *P* wave speed of 6.2 km/s for the entire crust, which is similar to the 5.9–6.1 km/s range from the Hi-CLIMB project located some 100–150 km to the east
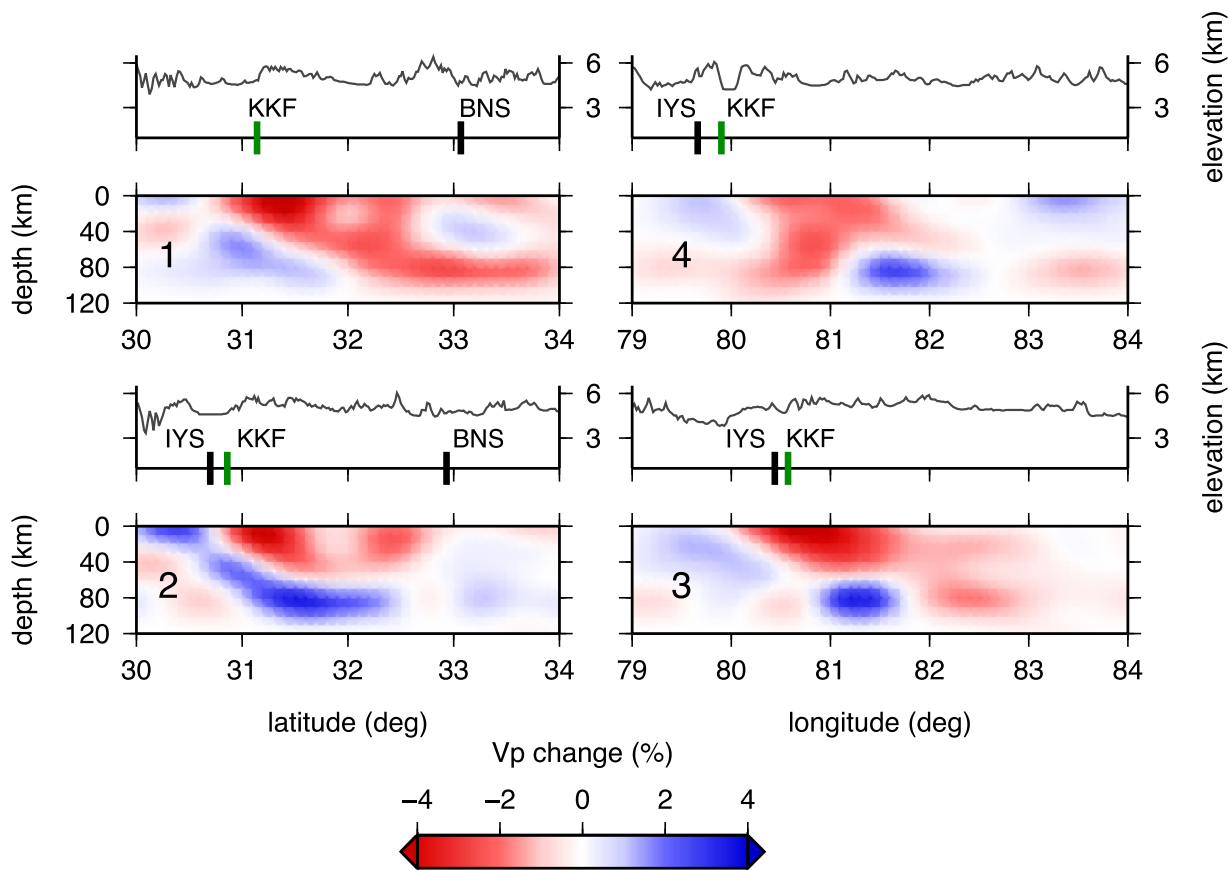
Figure 14. Vertical cross sections of the 3-D tomographic inversion in the well-resolved areas for *P* wave structure along N-S direction at (top left) 81°E, (bottom left) 81.5°E, and along E-W direction at (bottom right) 31.4°N and (top right) 32.2°N. Locations of the cross sections are shown in Figure 6. The topographic profile is shown above each plot. Black lines represent projections of the IYS and BNS sutures. Green lines show the projection of the Karakoram fault.

of our study area [*Griffin et al.*, 2011]. At the same time, it differs significantly from the results obtained further east in Tibet, where a layer of high (6.5 km/s or larger) *P* wave speed is reported at depths greater than 30 km [*Nelson et al.*, 1996; *Zhao et al.*, 2001; *Huang et al.*, 2009; *Zhang et al.*, 2011]. The 3.5 km/s *S* wave speed in our preferred 1-D model is at the high end of values reported by most studies of surface wave dispersion and ambient noise in the region [*Caldwell et al.*, 2009; *Yang et al.*, 2010], although *Rapine et al.* [2003] report even faster *S* waves in the lower crust along a profile through the Lhasa block.

The 1-D model also favors a crust-mantle transition at 75 km depth, which, because average elevations are about 4500 m, means that the crust here is about 80 km thick. This is smaller than the value reported by *Wittlinger et al.* [2004] for the northwestern part of our study area, but is only a few km thicker than values found along the Hi-CLIMB profile by *Nabelek et al.* [2009] and *Griffin et al.* [2011].

Tomographic images of the Tibetan crust are dominated by *P* wave speeds that are up to 4% slower than the mean (Figures 13 and 14). The lateral extent of the slow crustal anomaly (~200 km across) is significantly larger than the checkerboard elements we used to test the resolution (Figures 6 and 7), so we have confidence in our ability to resolve the shape of this feature. The anomaly is present through the entire depth range of the crust and is most pronounced above 30 km depth. While lateral resolution is poor in the upper crust, the association of the most intense part of the slow anomaly with the valley following the traces of the KKF and the IYS is not surprising.

In the cross sections (Figure 14), the slow crustal feature appears bowl shaped, i.e., it is wider at shallower depths. Low values of *P* wave speed appear primarily within the Lhasa block, and edges of the anomaly correlate well with tectonic boundaries (IYS and BNS) that define it [*Yin and Harrison*, 2000; *Murphy et al.*, 1997].

Due to limited resolution in the upper crust, the correlation of the low wave speed and the surface traces of major sutures is more confident for the depth range 30–70 km. This correlation is suggestive of the deep reach of the sutures separating distinct geological terraces of the Tibetan Plateau.

The southern and western edges of the slow anomaly show a distinct dip from the Himalaya into the Tibetan Plateau, while the northern and eastern boundaries of the feature are less clear. The crust beneath the Himalaya is consistently faster than the mean of our model. Restoration tests (Figure 12) indicate that we can resolve the sloping boundary that appears in the cross sections. Given its location with respect to major tectonic sutures and faults, the transition from the low speed under the Lhasa block to the faster material beneath the Himalaya likely represents the plate boundary between India and Eurasia. It should be noted that while in the map view the south-western limit of the slow anomaly appears to follow the trace of the KKF, west of ∼80°E our resolution is limited, and the shape may be artificially truncated due to the lack of rays.

Our finding of a well-defined boundary between volumes with very different properties is inconsistent with a significant exchange of crustal material between India and Eurasia envisaged by the "channel flow" scenario, but agrees with recent studies relying on different types of observations [*Klemperer et al.*, 2013; *Leech*, 2008] that describe the KKF as a crust-cutting fault. Therefore, the present-day low velocity under the Lhasa block is not likely a result of the India's ongoing collision with Eurasia, rather it may be related to the formation of the Lhasa block prior to the continental collision. In this context, it is important to note that the separation between the faster material beneath the Himalaya and the slower material beneath the Lhasa block is not vertical, but has a very distinct north and eastward slope. The shape suggests a thrust-type relationship, with the Lhasa block in the hanging wall. This conflicts with the well-documented strike-slip motion of the KKF, and likely points to a more complex stress transfer mechanism in the region [*Styron et al.*, 2011].

P wave speed values show no evidence of a distinct midcrustal low velocity zone in our study area, as may be expected in the "channel-flow" model of the Tibetan crust [*Klemperer*, 2006; *Royden et al.*, 2008]. Here our result is in agreement with a nearby study by *Griffin et al.* [2011], and with results reviewed in *Zhang et al.* [2011]. The presence of a low *P* wave velocity zone in the crust is revealed elsewhere beneath the plateau, most clearly in the southeastern part [*Nelson et al.*, 1996; *Klemperer*, 2006]. Results of a specifically designed resolution test (Figure 10) give us confidence in our ability to detect a low velocity feature, if there was one.

Our results show different patterns of the *P* wave speed anomalies in the crust and uppermost mantle. In the uppermost mantle, our tomographic images show a long, narrow fast *P* wave speed anomaly extending from the KKF in NE direction, crossing the BNS and merging with a broader fast anomaly that extends to the edge of the resolved volume (Figure 13). Beneath the Lhasa block, this narrow fast anomaly is surrounded by two low velocity features. The narrow fast anomaly appears to crosscut both the KKF and the BNS, while the prominent slow anomaly to the west of it crosses the BNS, but appears to stop at the KKF. Resolution tests using checkerboards and isolated larger features (Figures 6 and 11) confirm that the shape of the fast anomaly south of the BNS should be more reliable than to the north of it. The fast anomaly crosses the KKF, and the slow anomaly is truncated by it in the area (latitude range 31°N–32°N, longitude range 80°E–81.5°E) where we have especially good control over the lateral changes in the uppermost mantle (cf. Figures 6 and 11). Consequently, we consider these results reliable.

Fast velocities detected in the lower crust and the uppermost mantle of the Tibetan Plateau have been interpreted as evidence for a transformation of the mafic lower-crustal rocks into eclogite, a process that requires the Indian crust to be underthrust beneath the plateau. The presence of fast velocities [e.g., *Huang et al.*, 2009] or converting boundaries [*Schulte-Pelkum et al.*, 2005; *Nabelek et al.*, 2009] consistent with layers of fast velocity at crust-mantle boundary depth is often used as a guide to the northern extent of the Indian lithosphere.

The fast upper mantle anomaly we detect is similar in its properties to fast velocity features found in other studies. In vertical cross sections (Figure 14), it appears to connect to the shallower fast velocity feature in the crust, forming a ramp-flat geometry expected in the case of crustal underthrusting. The value of our absolute *P* wave speed at the depth of 90 km is ∼8.4 km/s, which is appropriate for eclogite at this depth [*Huang et al.*, 2009]. The presence of eclogite extending northward from the IYS in our study appears similar to the recent results from the Hi-CLIMB project ∼100 km to the east of our study area [*Nabelek et al.*, 2009;

Basuyau et al., 2013]. However, in our images the fast material extends farther north, and merges with a broader fast anomaly north of BNS. It is thus very interesting that the width of our fast anomaly in the east-west direction is only ~100 km. It is bound on both sides by much slower material and has a shape of a long narrow channel extending northeast from the India-Eurasia boundary. If indeed this feature represents eclogite formed due to the underthrusting of mafic lower-crustal material, this process is restricted to the narrow region of our study area.

Liang et al. [2012] combined multiple data sets available for the southeastern part of the Tibetan Plateau to constrain small-scale lateral variations in the upper mantle, which they interpreted as evidence of fragmentation in the Indian lithosphere. While our study lacks the depth resolution needed to reach a similar conclusion, we note a close similarity in the scale of lateral variation (~100 km) in our results and those of *Liang et al.* [2012]. Alternatively, localized formation of eclogite during the underthrusting of Indian crust may reflect the availability of material that can readily transform into it, and thus reflects the complexity in the geology of the downgoing Indian lithosphere.

A question that remains open is that of the fate of the upper-crustal rocks of India. If eclogite is formed from the faster lower-crustal rocks—where is the rest of the crustal column? Given that our results preclude a lateral transfer of material within the crust, the upper part of the Indian crust we conclude that it most likely is left behind and incorporated into the Himalaya.

11. Conclusions

Using regional seismic data observed by a network of portable seismographs over a period of 3 years, we have constructed a tomographic model of seismic velocity distribution in the crust and the uppermost mantle of western Tibet. Our results cover an area previously not sampled at the regional scale. Through a series of resolution tests we confirmed that we have sufficient sensitivity to the absolute values of seismic wave speed, that we can resolve lateral changes on the order of 70 km and vertical changes on the order of 20 km, and that our inversion procedures do not introduce artifacts in areas where we have no resolution.

We find the crust of western Tibet to be consistently slower than the crust of the Himalaya. The boundary separating the crustal volumes with different speed generally follows the trace of the KKF, and dips to the north and east. The crust of the Tibetan Plateau appears remarkably uniform throughout its ~80 km thickness, with neither a lower-crustal increase in speed nor any evidence of a midcrustal zone with reduced wave speed. In the uppermost mantle, a prominent narrow fast feature cuts across major tectonic boundaries (KKF, BNS). In cross section, the sloping boundary separating faster Himalayan crust from the slower Tibetan one merges with the upper mantle fast feature to form a characteristic ramp-flat structure.

Our findings show western Tibetan crust to be considerably different from that in central and eastern parts of the plateau. Both the subvertical boundary delimiting its southern and western extent, and the lack of evidence for the midcrustal low wave speed zone argue against ductile deformation in the form of channel flow in western Tibet. We contend that the inclined boundary separating faster and slower crustal volumes, and tracking the KKF, corresponds to the plate boundary between India and Eurasia at depth. Consequently, the ramp-flat shaped fast wave speed body we image reflects the process of underthrusting of the Indian crust beneath Tibet. The northernmost extent of this feature in our images is 32.5°N. Significantly, the lateral changes in the upper mantle wave speed suggest variability in either the process of underthrusting, or in the nature of the material involved, along the strike of the India-Himalaya boundary. Specifically, if the fast upper mantle feature represents rocks from the lower crust of India being underthrust, and eclogitized beneath Tibet, then this process is highly nonuniform along the India-Eurasia collision boundary.

References

Basuyau, C., M. Diament, C. Tiberi, G. Hetényi, J. Vergne, and A. Peyrefitte (2013), Joint inversion of teleseismic and GOCE gravity data: Application to the Himalayas, *Geophys. J. Int.*, *193*(1), 149–160, doi:10.1093/gji/ggs110.
Bilham, R. (2004), Earthquakes in India and the Himalaya: Tectonics, geodesy and history, *Ann. Geophys.*, *47*, 839–858.
Burchfiel, B. C., and L. H. Royden (1985), North-south extension within the convergent Himalayan region, *Geology*, *13*, 679–682.
Caldwell, W. B., S. L. Klemperer, S. S. Rai, and J. F. Lawrence (2009), Partial melt in the upper-middle crust of the northwest Himalaya revealed by Rayleigh wave dispersion, *Tectonophysics*, *477*(1), 58–65.
Copley, A., and D. McKenzie (2007), Models of crustal flow in the India-Asia collision zone, *Geophys. J. Int.*, *169*, 683–698.

Dricker, I. G., and S. W. Roecker (2002), Lateral heterogeneity in the upper mantle beneath the Tibetan Plateau and its surroundings from SS-S travel time residuals, *J. Geophys. Res.*, *107*(B11), 2305, doi:10.1029/2001JB000797.

Griffin, J. D., R. L. Nowack, W. P. Chen, and T. L. Tseng (2011), Velocity structure of the Tibetan Lithosphere: Constraints from P-wave travel times of regional earthquakes, *Bull. Seismol. Soc. Am.*, *101*(4), 1938–1947, doi:10.1785/0120100229.

Hearn, T. (1999), Uppermost mantle velocities and anisotropy beneath Europe, *J. Geophys. Res.*, *104*(B7), 15,123–15,139.

Huang, G. C., F. T. Wu, S. W. Roecker, and A. F. Sheehan (2009), Lithospheric structure of the central Himalaya from 3-D tomographic imaging, *Tectonophysics*, *475*, 524–543, doi:10.1016/j.tecto.2009.06.023.

Kapp, P., M. A. Murphy, A. Yin, T. M. Harrison, L. Ding, and J. Guo (2003), Mesozoic and Cenozoic tectonic evolution of the Shiquanhe area of western Tibet, *Tectonics*, *22*(4), 1029, doi:10.1029/2001TC001332.

Kapp, P., P. G. DeCelles, G. Gehrels, M. Heizler, and L. Ding (2007), Geological records of the Lhasa-Qiangtang and Indo-Asian collisions in the Nima area of central Tibet, *Geol. Soc. Am. Bull.*, *119*, 917–932.

Klemperer, S. L. (2006), Crustal flow in Tibet: Geophysical evidence for the physical state of Tibetan lithosphere, and inferred patterns of active flow, in *Channel Flow, Ductile Extrusion and Exhumation in Continental Collision Zones*, edited by Law, R. D., M.P. Searle, and L. Godin, *Geol. Soc. Lond. Special Publication*, v. 268, 39–70.

Klemperer, S. L., B. M. Kennedy, S. R. Sastry, Y. Makovsky, T. Harinarayana, and M. L. Leech (2013), Mantle fluids in the Karakoram fault: Helium isotope evidence, *Earth Planet. Sci. Lett.*, *366*, 59–70, doi:10.1016/j.epsl.2013.01.013.

Kosarev, G., R. Kind, S. V. Sobolev, X. Yuan, W. Hanka, and S. Oreshin (1999), Seismic evidence for detached Indian lithospheric mantle beneath central Tibet, *Science*, *283*, 1306–1308.

Leech, M. L. (2008), Does the Karakoram fault interrupt mid-crustal channel flow in the western Himalaya?, *Earth Planet. Sci. Lett.*, *276*, 314–322, doi:10.1016/j.epsl.2008.10.006.

Li, C., R. D. Van der Hilst, A. S. Meltzer, and E. R. Engdahl (2008), Subduction of the Indian lithosphere beneath the Tibetan Plateau and Burma, *Earth Planet. Sci. Lett.*, *274*(1–2), 157–168, doi:10.1016/j.epsl.2008.07.016.

Li, S., W. D. Mooney, and J. Fan (2006), Crustal structure of mainland China from deep seismic sounding data, *Tectonophysics*, *420*, 239–252.

Liang, X., E. Sandvol, J. Chen, T. Hearn, J. Ni, S. Klemperer, Y. Shen, and F. Tilmann (2012), A complex Tibetan upper mantle: A fragmented Indian slab and no south-verging subduction of Eurasia lithosphere, *Earth Planet. Sci. Lett.*, *333–334*, 101–111.

Molnar, P. (1984), Structure and tectonics of the Himalaya: Constraints and implications of geophysical data, *Annu. Rev. Earth Planet. Sci.*, *12*, 489–518.

Molnar, P., and P. Tapponnier (1975), Cenozoic tectonics of Asia: Effects of a continental collision, *Science*, *189*, 419–426.

Murphy, M. A., et al. (1997), Did the Indo-Asian collision alone create the Tibetan plateau?, *Geology*, *25*, 719–722.

Nabelek, J., et al. (2009), Underplating in the Himalaya-Tibet collision zone revealed by the Hi-CLIMB experiment, *Science*, *325*, 1371–1374.

Nelson, K. D., et al. (1996), Partially molten middle crust beneath southern Tibet: Synthesis of project 26INDEPTH results, *Science*, *274*, 1684–1688.

Rapine, R., F. Tilmann, M. West, J. Ni, and A. Rodgers (2003), Crustal structure of northern and southern Tibet from surface wave dispersion analysis, *J. Geophys. Res.*, *108*(B2), 2120, doi:10.1029/2001JB000445.

Roecker, S., C. Thurber, and D. McPhee (2004), Joint inversion of gravity and arrival time data from Parkfield: New constraints on structure and hypocenter locations near the SAFOD drill site, *Geophys. Res. Lett.*, *31*, L12S04, doi:10.1029/2003GL019396.

Roecker, S. W., C. Thurber, K. Roberts, and L. Powell (2006), Refining the image of the San Andreas Fault near Parkfield, California using a finite difference travel time computation technique, *Tectonophysics*, *426*, 189–205.

Royden, L. H., B. C. Burchfiel, and R. D. van der Hilst (2008), The geological evolution of the Tibetan Plateau, *Science*, *321*, 1054–1058, doi:10.1126/science.1155371.

Schulte-Pelkum, V., G. Monsalve, A. Sheehan, M. R. Pandey, S. Sapkota, R. Bilham, and F. Wu (2005), Imaging the Indian subcontinent beneath the Himalaya, *Nature*, *435*, 1222–1225.

Searle, M. P., J. R. Elliott, R. J. Phillips, and S.-L. Chung (2011), Crustal-lithospheric structure and continental extrusion of Tibet, *J. Geol. Soc.*, *168*, 633–672.

Styron, R., M. Taylor, and M. Murphy (2011), Oblique convergence, arc parallel extension, and strike-slip faulting in the high Himalaya, *Geosphere*, *7*(2), 1–15, doi:10.1130/GES00606.1.

Sun, X. L., X. D. Song, S. H. Zheng, Y. J. Yang, and M. H. Ritzwoller (2010), Three dimensional shear wave velocity structure of the crust and upper mantle beneath China from ambient noise surface wave tomography, *Earthquake Sci.*, *23*, 449–463.

van Hinsbergen, D. J. J., P. Kapp, G. Dupont-Nivet, P. C. Lippert, P. G. DeCelles, and T. H. Torsvik (2011), Restoration of Cenozoic deformation in Asia, and the size of Greater India, *Tectonics*, *30*, TC5003, doi:10.1029/2011TC002908.

Wessel, P., and W. H. F. Smith (1991), Free software helps map and display data, *Eos Trans. AGU*, *72*(441), 445–446.

Wittlinger, G., J. Vergne, P. Tapponnier, V. Farra, G. Poupinet, M. Jiang, H. Su, G. Herquel, and A. Paul (2004), Teleseismic imaging of subducting lithosphere and Moho offsets beneath western Tibet, *Earth Planet. Sci. Lett.*, *221*, 117–130.

Yang, Y., et al. (2010), Rayleigh wave phase velocity maps of Tibet and the surrounding regions from ambient seismic noise tomography, *Geochem. Geophys. Geosyst.*, *11*, Q08010, doi:10.1029/2010GC003119.

Yin, A., and T. M. Harrison (2000), Geologic evolution of the Himalayan-Tibetan orogen, *Annu. Rev. Earth Planet. Sci.*, *28*, 211–280, doi:10.1146/annurev.earth.28.1.211.

Zhang, H., S. Roecker, C. H. Thurber, and W. Wang (2012), Seismic imaging of microblocks and weak zones in the crust beneath the southeastern margin of the Tibetan plateau, in *Earth Sciences*, edited by I. A. Dar, InTech, Croatia. [Available at http://www.intechopen.com/books/earth-sciences/seismic-imaging-of-microblocks-and-weak-zones-in-the-crust-beneath-the-southeastern-margin-of-the-ti.]

Zhang, Z., Y. Deng, J. Teng, C. Wang, R. Gao, Y. Chen, and W. Fan (2011), An overview of the crustal structure of the Tibetan plateau after 35 years of deep seismic soundings, *J. Asian Earth Sci.*, *40*, 977–989, doi:10.1016/j.jseaes.2010.03.010.

Zhao, W., et al. (2001), Crustal structure of the central Tibet as derived from project INDEPTH wide-angle seismic data, *Geophys. J. Int.*, *145*, 486–498.